# Quantifying spatial distribution of spurious mixing in ocean models

Mehmet Ilıcak [a,*]

[a] *Uni Research Climate, Bjerknes Centre for Climate Research, Bergen, Norway*

**Abstract**

Numerical mixing is inevitable for ocean models due to tracer advection schemes. Until now, there is no robust way to identify the regions of spurious mixing in ocean models. We propose a new method to compute the spatial distribution of the spurious diapycnic mixing in an ocean model. This new method is an extension of available potential energy density method proposed by Winters and Barkan (2013). We test the new method in lock-exchange and baroclinic eddies test cases. We can quantify the amount and the location of numerical mixing. We find high-shear areas are the main regions which are susceptible to numerical truncation errors. We also test the new method to quantify the numerical mixing in different horizontal momentum closures. We conclude that Smagorinsky viscosity has less numerical mixing than the Leith viscosity using the same non-dimensional constant.

*Key words:* Spurious diapycnic mixing; lock-exchange; reference potential energy; Leith viscosity

## 1 Introduction

This paper provides a novel method that quantifies the spatial distribution of spurious diapycnic mixing in numerical models of ocean circulation. We update the study of Ilıcak et al. (2012) that employed the reference potential energy methods to measure spurious mixing in ocean general circulation models.

* Corresponding author. Mehmet Ilıcak. Uni Research Climate, Allegt. 55 5007, Bergen, Norway

*Email address:* mehmet.ilicak@uni.no (Mehmet Ilıcak).

State-of-the-art ocean models have spurious diapycnic (cross-density) mixing due to truncation errors in the discrete tracer advection schemes (Griffies et al., 2000; Ilıcak et al., 2012) and/or cabbeling which is arising from the nonlinearity of the equation of state for seawater (McDougall, 1987; IOC et al., 2010). Ilıcak et al. (2012) showed that all type vertical coordinate ocean models (geopotential, terrain following and isopycnic coordinate) suffer from spurious diapycnic mixing due to cabbeling, while geopotential and terrain following coordinate models suffer from numerical mixing due to advection schemes.

There are various methods that have been used to diagnose spurious mixing in ocean models. Griffies et al. (2000) quantified spurious mixing in idealized basin scale simulations and suggested that it may be significant for large scale ocean climate. Ilıcak et al. (2012) examined four idealized test cases and measured the spurious diapycnic mixing using the evolution of reference potential energy (RPE) proposed by Winters et al. (1995). The idealized test cases are; i) lock exchange, ii) overflow, iii) internal wave, and iv) baroclinic eddies. These cases progress from simple domains and initial conditions to more complex dynamics and topography, so that spurious mixing may be measured under a variety of conditions. Ilıcak et al. (2012) found that grid Reynolds number and momentum advection scheme are as important as the choice of tracer advection scheme. They concluded that different momentum closures might lead to different amounts of spurious mixing. Recently, Petersen et al. (2015) performed the same test cases with the Model for Prediction Across Scales-Ocean (MPAS-Ocean) using the arbitrary Lagrangian-Eulerian method in the vertical. An alternative approach was suggested by Burchard and Rennau (2008), based on the variance decay induced by the tracer advection scheme to quantify local numerical mixing. However, their method does not distinguish between isopycnic (along-density) and diapycnic mixing. Later, Urakawa and Hasumi (2014) quantified numerical mixing in terms of spurious water mass transformation rates. Despite the progress in developing the diagnostic methods of numerical mixing and dissipation, all the studies reviewed so far, however, could not answer the most important question; *where does spurious mixing occur?*

In this study, we propose a new method that can quantify the spatial distribution of the spurious mixing in an ocean model. We test the new method using the lock-exchange and baroclinic eddies test cases described by Ilıcak et al. (2012) with the MIT general circulation model (MITgcm, Marshall et al. (1997)). To our knowledge, this is the first time that a method that computes the location of spurious diapycnic mixing is provided. The aim of this paper is to address the following questions;

(1) can the proposed method compute the spatial distribution of spurious

mixing? in which regions can spurious diapycnic mixing be high?
(2) will different momentum closures make a difference in spurious mixing?

The new method is an extension of the available potential energy density method described by Winters and Barkan (2013). We refer to the new method as the reference potential energy density (RPED) method. We find out that RPED diagnoses the spurious mixing regions to coincide with high-shear regions. Section 2 describes this new method used to diagnose the regions of spurious diapycnic mixing. Sections 3.1 and 3.2 present results and analysis for the idealized test cases consisting of a lock-exchange, and baroclinic eddies in a channel, respectively. We present our conclusions in Section 4.

## 2 Resting Potential Energy Density method

In this section, we describe the new method. First we describe basic energy terms of a system such as potential energy, available potential energy and reference potential energy. Then we describe available potential energy density method proposed by Winters and Barkan (2013). Finally, we extend their method to compute spurious diapycnic mixing.

The total potential energy (PE) of a fluid is calculated as the volume integral of the density-weighted geopotential:

$$PE(t) = g \iiint \rho \, z \, \mathrm{d}V. \tag{1}$$

Following Winters and Barkan (2013), the available potential energy (APE) is defined in terms of the reference profile $\rho(z^*)$ where $z^*$ is the equilibrium height of a fluid parcel with potential density $\rho$. This leads to

$$APE(t) = g \iiint \rho \, (z - z^*) \, \mathrm{d}V. \tag{2}$$

The definition of reference potential energy is therefore simply

$$RPE(t) = PE - APE \tag{3}$$

$$RPE(t) = g \iiint \rho \, z^* \, \mathrm{d}V. \tag{4}$$

Winters and Barkan (2013) defined a new term, namely available potential energy density $\mathcal{E}_{APE}$

$$\mathcal{E}_{APE}(\mathbf{x},t) = (z - z^*)(\rho(\mathbf{x},t) - \bar{\rho}(z,z^*)), \tag{5}$$

where

$$\bar{\rho}(z,z^*) = \frac{1}{(z-z^*)} \int_{z^*}^{z} \rho(z^{*\prime}) dz^{*\prime}. \tag{6}$$

They showed that the available potential energy density has two properties:

$$g \iiint \mathcal{E}_{APE}(\mathbf{x},t) dV = APE(t) \tag{7}$$

$$\mathcal{E}_{APE}(\mathbf{x},t) \geq 0 \qquad \forall \mathbf{x}, t. \tag{8}$$

We can re-write the definition of APE using Eqs. 5 and 7 as

$$APE(t) = g \iiint (z - z^*)\rho(\mathbf{x},t) dV - g \iiint \left( \int_{z^*}^{z} \rho(z^{*\prime}) dz^{*\prime} \right) dV. \tag{9}$$

Denoting the terms on the right hand side (RHS) in Eq. 9 as $\Gamma_1$ (the first term on the RHS) and $\Gamma_2$ (the second term on the RHS) respectively, Winters and Barkan (2013) proved that global sum of $\Gamma_2$ is equal to zero in the domain. Thus, Eq. 9 recovers the original equation described above (Eq. 2). Winters and Barkan (2013) also defined $\Gamma$ terms for each $i$th parcel with volume element $dV_i$ located at height $z_i$ with density $\rho_i$ as

$$\Gamma_1^i = g dV_i \rho_i (z_i - z_i^*) \tag{10}$$

$$\Gamma_2^i = -g \Delta z^* \sum_{j=1}^{n} \rho_j dV_i, \tag{11}$$

where $n$ is the number of $dV$ parcels with height in the reference density profile between $z_i^*$ and $z_i$. The $z_i^*$ term is the equilibrium position of the parcel $i$th (i.e. $z_i^* = z^*(\rho_i)$), and the increment $\Delta z^*$ is a signed quantity with a magnitude $dz^* = dV/A$. Winters and Barkan (2013) employed $\mathcal{E}_{APE}$ to compute a three dimensional structure of available potential energy in the system (see their figure 5).

Here we extend their work by defining a new quantity called reference potential energy density, $\mathcal{E}_{RPE}$, as

$$\mathcal{E}_{RPE}(\mathbf{x},t) = z^* \rho(\mathbf{x},t) + \int_{z^*}^{z} \rho(z^{*\prime}) dz^{*\prime}. \tag{12}$$

The second term in Eq. 12 is the opposite sign of second term in Eqs. 5 and 9. This new quantity has the property of $g \int \mathcal{E}_{RPE}(\mathbf{x}, t) dV = RPE(t)$ which leads to

$$RPE(t) = g \iiint z^* \rho(\mathbf{x}, t) dV + g \iiint \left( \int_{z^*}^{z} \rho(z^{*\prime}) dz^{*\prime} \right) dV, \tag{13}$$

$$RPE(t) = \Gamma_3 + \Gamma_2. \tag{14}$$

It can be easily shown that sum of Eqs. 9 and 13 is equal to the total potential energy, PE (Eq. 1).

The reference potential energy density is a 4D field (x,y,z,t) and the change of $\mathcal{E}_{RPE}$ over a time increment $(t, t + \Delta t)$ shows regions where absolute reference potential energy increased in the system due to diapycnic mixing. Since the diapycnic mixing is irreversible, absolute reference potential energy change has to be positive definite. The only caveat is that we also need to take into account advection of $\mathcal{E}_{RPE}$ in time;

$$\frac{d\mathcal{E}_{RPE}}{dt} = \frac{\partial \mathcal{E}_{RPE}}{\partial t} + \mathbf{u} \cdot \nabla_H \mathcal{E}_{RPE} + w \frac{\partial \mathcal{E}_{RPE}}{\partial z}, \tag{15}$$

where $d/dt$ is the material derivative, $\mathbf{u}$ is the two dimensional horizontal velocity, $\nabla_H$ is the horizontal gradient operator and $w$ is the vertical velocity (see Appendix).

We present results from this new method in the next section. The advantages of this new method are i) it works on energetics rather than ''effective'' diffusivity, ii) it can be implemented both on line and off line which saves computational time, iii) it shows the regions of spurious and explicit mixing.

## 3 Results

We show results from two different model experiments; i) 2D lock-exchange ii) 3D baroclinic eddies in a periodic channel. We test the new $\mathcal{E}_{RPE}$ method using the MIT general circulation model (MITgcm). The MITgcm is a three dimensional C-grid ocean code using fully incompressible (the Boussinesq approximation) Navier Stokes equations (Marshall et al., 1997). Here we employ the MITgcm with the $z-$level coordinate formulation, a linear equation of state and the hydrostatic approximation. In addition, convective adjustment and explicit diffusion parameterizations are turned-off, if it is not mentioned otherwise.

### 3.1 Lock-exchange

The model configuration is similar to the non-rotating gravitational adjustment problem described in Haidvogel and Beckmann (1999) and Ilıcak et al. (2012). The computational domain is two-dimensional, with horizontal dimension $0 \leq x \leq L$ and vertical dimension $-H \leq z \leq 0$, where $L = 64$ km and $H = 20$ m. Insulated boundary conditions are used for temperature and salinity on all boundaries, and free-slip boundary conditions for velocity components. The lock-exchange problem is initialized with dense (cold) fluid on the left separated from the light (warm) fluid on the right (see Figure 1 (a)). Salinity remains a constant at 35 psu throughout the domain, with density a linear function of temperature. The initial density contrast ($\delta\rho$) across the vertical front is 5 kg m$^{-3}$. The horizontal and vertical grid spacings are 500 m and 1 m, respectively. A third order monotonic upwind biased tracer advection scheme is used for temperature equation. More details about the model setup can be found in Ilıcak et al. (2012).

We conduct two different simulations. The first run (*Exp*1) is with no explicit horizontal and vertical diffusion (i.e. $\kappa_h = \kappa_v = 0$), and we test the new method to diagnose regions of spurious mixing. The second simulation (*Exp*2) is performed using a constant vertical diffusivity ($\kappa_v = 1 \times 10^{-4}$ m$^2$/s), and we compare the results between the two simulations.

#### 3.1.1 Simulation without explicit diffusion

There are only two density classes at the initial time for the lock-exchange case ($\rho_1 = 1027$ kg m$^{-3}$ and $\rho_2 = 1022$ kg m$^{-3}$ in Fig. 1 (a)). The initial state of the available potential energy density field is shown in Fig. 2 (a). The $\mathcal{E}_{APE}$ is positive-definite as expected everywhere in the domain. There are two regions where $\mathcal{E}_{APE}$ is non-zero and these are the regions where the two fronts (heads of gravity currents) will propagate in time. The $\mathcal{E}_{APE}$ field is consistent with the one Winters and Barkan (2013) described in their study. Figure 1 (b) shows the density field of the MITgcm simulation with zero explicit diffusivity (*Exp*1) at time=0.5 hours. The initial vertical front started to separate into left and right propagating fronts. A slight change in the $\mathcal{E}_{APE}$ field can be seen in Fig. 2 (b).

Two well-defined fronts are visible in the domain at time=10 hours (Fig. 1 (c)). It is clearly seen that new density classes (yellow, cyan and orange colors) are formed as the fronts widen. This is due to spurious mixing of the tracer advection (Ilıcak et al., 2012). The $\mathcal{E}_{APE}$ fields are plotted in Fig. 2 (c) at the same time. Most of the APE between $x \approx 16$ km and $x \approx 48$ km has been converted into kinetic energy. Some of the APE remains close to the side

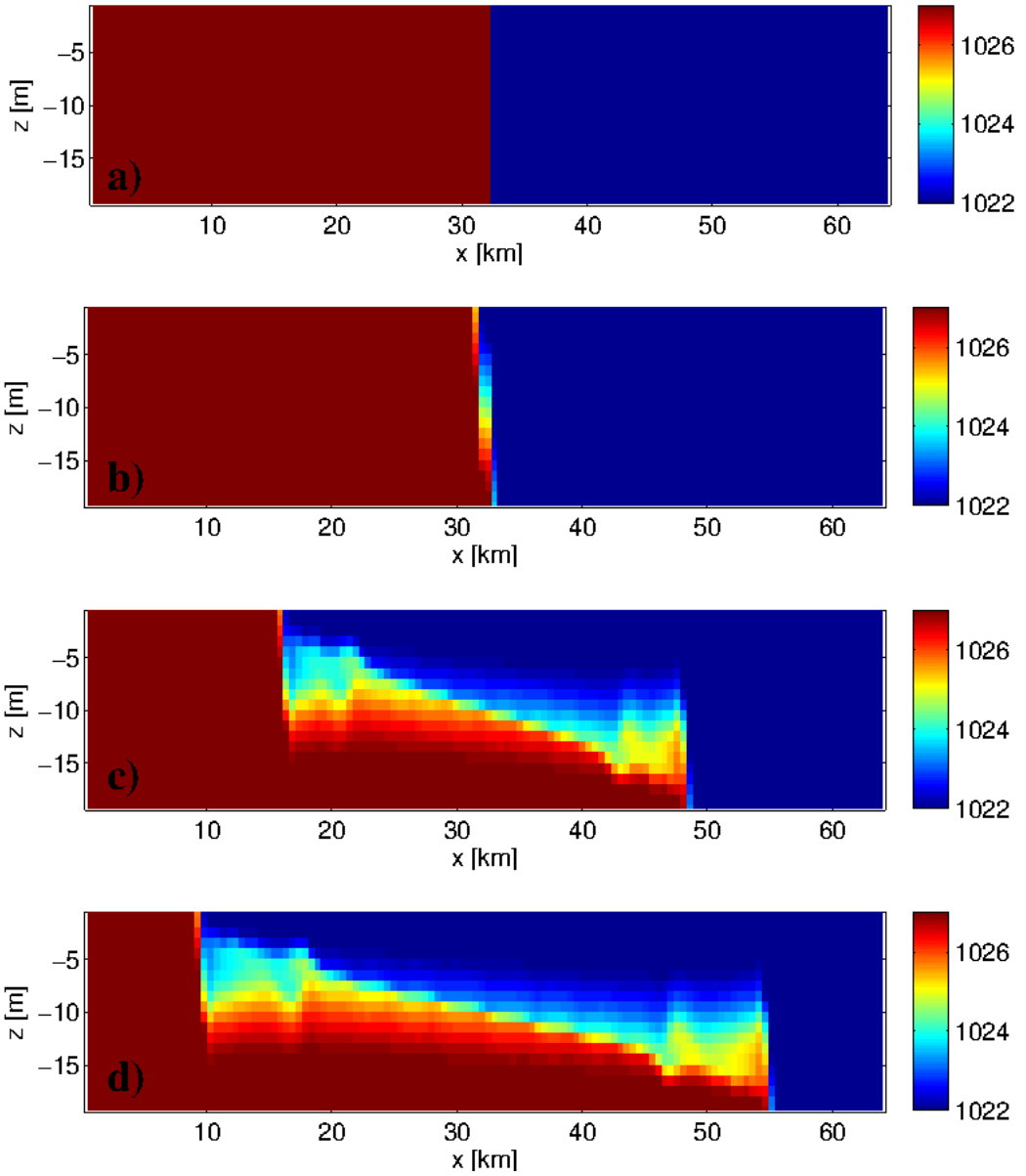


Fig. 1. (a) Initial density field for the lock-exchange test case. Density [kg m$^{-3}$] for the MITgcm simulation with no explicit diffusion after; (b) 0.5 hours, (c) 10 hours, (d) 14 hours of simulation.

walls, this indicates that fronts will keep flowing along that direction. The upper and lower fronts propagate approximately 6 km and reach to $x \approx 10$ km and $x \approx 54$ km, respectively at time=14 hours (Fig. 1 (d)).

Figure 2 (e) displays the change of the reference potential energy density field between $t = 14$ hours and $t = 0$ (i.e. $\Delta\mathcal{E}_{RPE} = \mathcal{E}_{RPE}(\mathbf{x}, t = 14$ hours$) - \mathcal{E}_{RPE}(\mathbf{x}, t = 0)$). There are two regions symmetric but with opposite signs in the $\Delta\mathcal{E}_{RPE}$ field. Positive/negative sign indicates that dense/light water is replaced by light/dense water. One should be careful how to inter-

pret this picture. This field contains both spurious diapycnic mixing which we are after and also advection of the $\mathcal{E}_{RPE}$ field in time. To quantify only the spurious mixing part, next we remove the contribution from advection terms. We employ first order upwind advection scheme to the $\mathcal{E}_{RPE}$ field to compute the advection terms off-line.

We compute the total amount of diapycnic mixing using $\int_{\tau=t_1}^{\tau=t_2}(d\mathcal{E}_{RPE}/dt)d\tau$ in two different time slices. Figure 3 shows the regions of total amount of spurious mixing; (a) between $t_1 = 0$ hours and $t_2 = 0.5$ hours (upper panel), (b) between $t_1 = 10$ hours and $t_2 = 14$ hours (lower panel). The regions where numerical mixing occurs coincide with the propagating head of two fronts where high-shear values are observed. This is possibly due to high grid Reynolds numbers in those regions because of large vertical and horizontal velocities. There are two primary regions of spurious diapycnic mixing in Fig. 3 (b). These are near the vertical head of the gravity currents and lateral interface behind the two fronts. The light/heavy water in front of the gravity current head has to displace up/down such that lateral flow is strongly divergent. Ilıcak et al. (2012) described this phenomena in a sketch.

This is the first time we can quantify the amount of mixing in these regions. When we sum the $d\mathcal{E}_{RPE}/dt$ field in time, we recover total change of RPE which is shown as the red line in Fig. 5 which will be discussed later. The RPE changes only via diapycnic mixing in a closed system, with mixing increasing the RPE (Winters et al., 1995; Ilıcak et al., 2009). The diagnosed spurious mixing field is not fully symmetric. The reason behind this might be the off-line computation using a lower order advection scheme for the $\mathcal{E}_{RPE}$. Higher order advection and on-line calculation might improve the accuracy of the $\mathcal{E}_{RPE}$, however this is beyond the scope of this study. Here we want to show that the new method can diagnose the spatial distribution of spurious mixing.

### *3.1.2 Simulation with explicit diffusion*

Next we test the new method to separate the total mixing into spurious and physical contributions. To do so, a new lock-exchange experiment with an explicit vertical diffusion of $\kappa_v = 10^{-4}$ m$^2$/s is conducted (*Exp*2). Hughes et al. (2009) showed that physical (explicit) irreversible mixing ($\Phi_{irr}$) can be computed using

$$\Phi_{irr}(\mathbf{x}, t) = gz^* \frac{\partial}{\partial z}\left[\kappa_v \frac{\partial \rho}{\partial z}\right] dV. \tag{16}$$

Spatial distributions of total, explicit irreversible, and spurious mixing in the

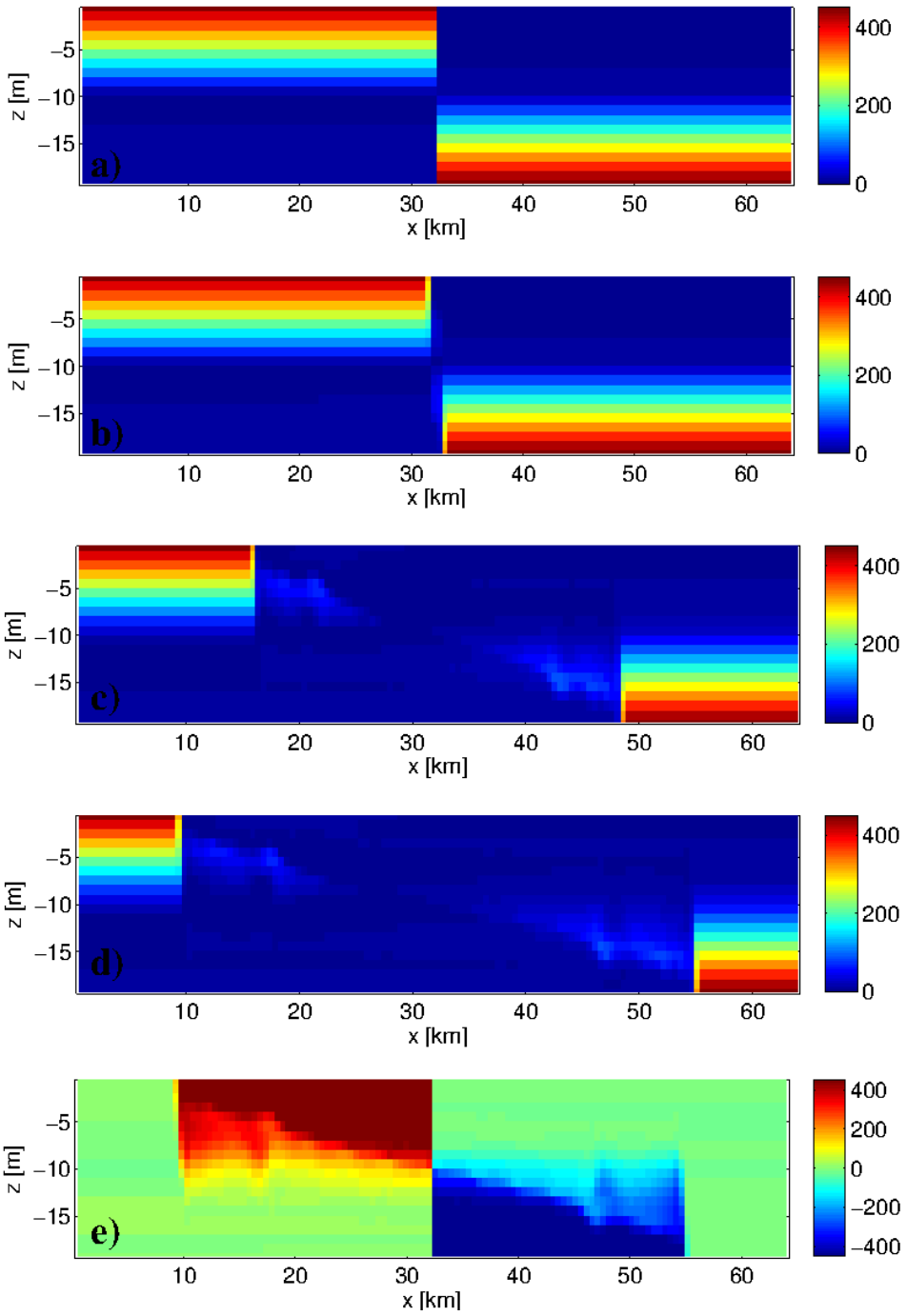


Fig. 2. MITgcm simulation for the lock-exchange test case with no explicit diffusion: (a) Initial available potential energy density ($\mathcal{E}_{APE}$). Snapshot of $\mathcal{E}_{APE}$ at (b) time=0.5 hours, (c) time= 10 hours, (d) time= 14 hours. (e) Change of the reference potential energy density ($\mathcal{E}_{RPE}$) between time= 14 hours and time= 0. All units are in kg $m^{-1}s^{-2}$.

*Exp*2 case are shown in Figure 4 (a), (b) and (c), respectively between time=10 and time=14 hours. The explicit amount of mixing is limited between $x \approx 10$

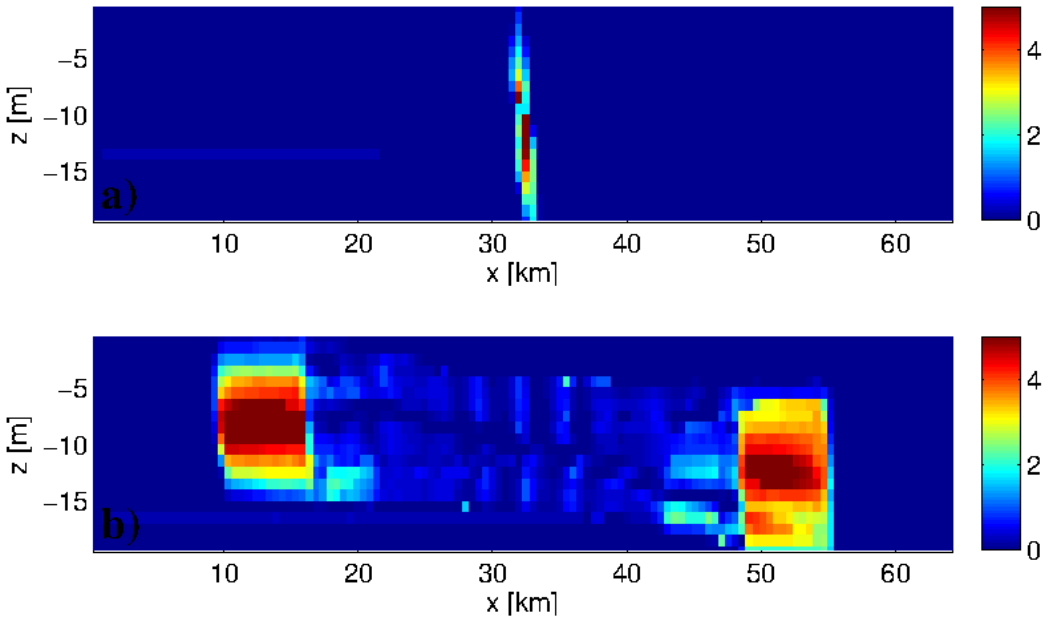


Fig. 3. MITgcm simulation for the lock-exchange test case with no explicit diffusion, *Exp*1: (a) total amount of spurious mixing between time=0 and time=0.5 hours. (b) total amount of spurious mixing between time=10 and time=14 hours. All units are in kg $m^{-1}s^{-1}$.

km and $x \approx 54$ km, since vertical density gradient is only in that region (Fig. 4 b). The total amount of spurious mixing in the *Exp*2 case (Fig. 4 c) is similar to the one in the *Exp*1 simulation (Fig. 3 b). Note that the amount of explicit mixing is an order of magnitude smaller than the spurious mixing.

Figure 5 displays the normalized cumulative RPE change in time (volume integral of $\mathcal{E}_{RPE}$) for *Exp*1 and *Exp*2 simulations. The total amount of mixing in the *Exp*2 case (blue line) is larger than total mixing in the *Exp*1 case (red line), since additional explicit diffusion increases the diapycnic mixing in the *Exp*2 case. The amount of explicit diapycnic mixing, which is computed using Eq. 16, in the *Exp*2 case (green line) is increasing in time due to irreversible mixing. The numerical mixing in the *Exp*2 case is simply the difference between total and explicit amount of mixing. This is plotted as the black line in the same figure. It can be seen that the black line follows the red line closely. This indicates that amounts of spurious mixing in both experiments are close to each other.

The new reference potential energy density method can successfully quantify the spatial distribution of total and spurious mixing in a closed system. We find out that spurious mixing *cannot* be suppressed by explicit mixing. Both no diffusivity and constant vertical diffusivity experiments show similar amount of spurious mixing. This was also observed by Ilıcak et al. (2012). In their global simulations, they found sensitivities to changing $\kappa_v$ from 0 to

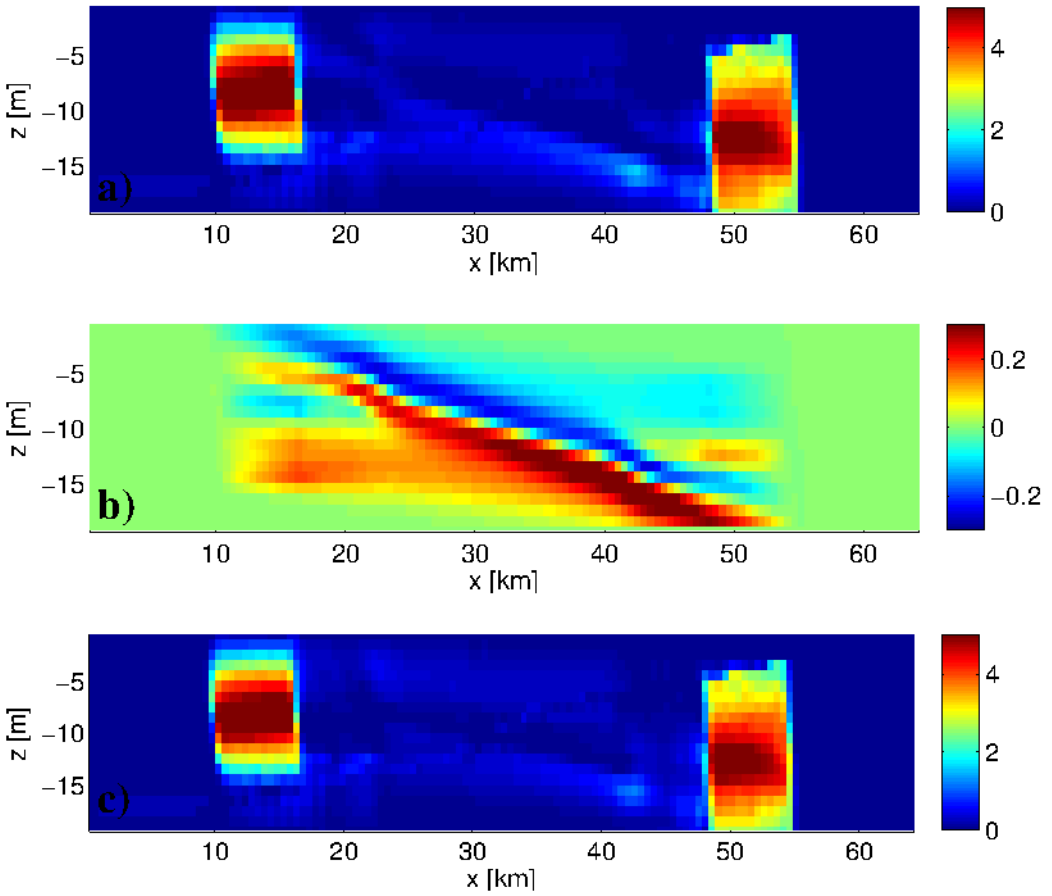


Fig. 4. MITgcm simulation for the lock-exchange test case with explicit diffusion, *Exp*2: (a) total amount of mixing between time=10 and time=14 hours. (b) total amount of irreversible mixing between time=10 and time=14 hours. (c) total amount of spurious mixing between time=10 and time=14 hours. All units are in kg $m^{-1}s^{-1}$.

$10^{-6}$ $m^2/s$ and yet have levels of spurious mixing that are much larger than these changes.

### *3.2 Baroclinic eddies test case*

Here we investigate spurious mixing regions in a channel with three-dimensional baroclinic eddies. The domain consists of a horizontally periodic channel of latitudinal extent 500 km and longitudinal extent 160 km, with a flat bottom of 1000 m depth. The channel is on an $f-$plane with the Coriolis parameter $f = 1.2\times10^{-4}\,s^{-1}$ (roughly 55°N latitude). The initial temperature interface on the horizontal between north and south of the channel is a cosine shape with a wavelength of $x = 120$ km (Fig. 6 a). The initial temperature profile is uniformly decreasing in the vertical with a horizontal

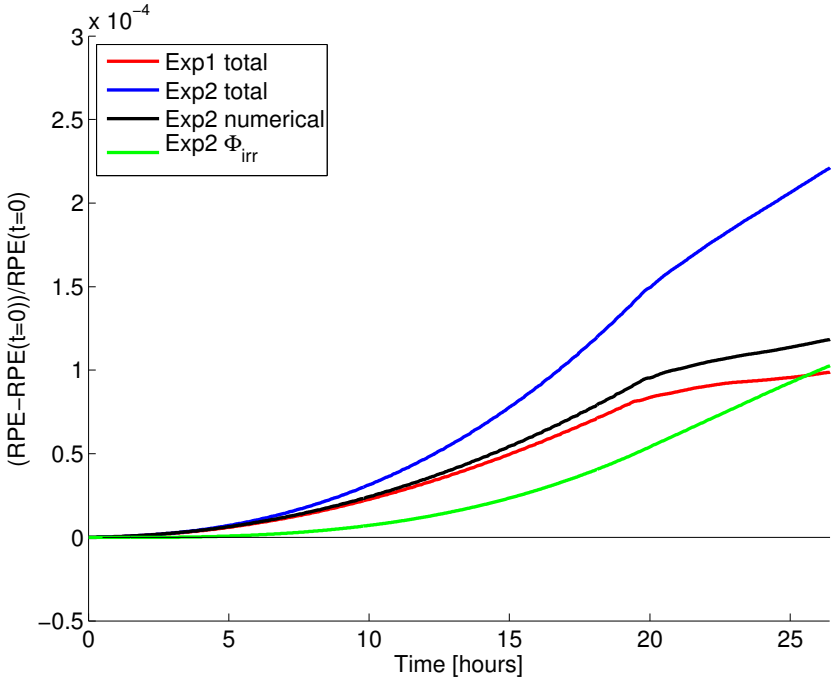


Fig. 5. Normalized reference potential energy vs time for zero diffusivity and $\kappa_v = 10^{-4}$ m$^2$/s cases.

gradient at the channel center (Fig. 6 b). A quadratic bottom drag is used with dimensionless drag coefficient of $C_d = 0.01$. The large bottom drag coefficient and asymmetric initial condition promote baroclinic instability in the channel (Ilıcak et al., 2012). The first baroclinic Rossby radius of deformation is 20 km. The horizontal grid spacing is 4 km which we interpret as mesoscale eddy permitting. Vertical grid resolution is constant and 50 meters. Salinity is kept constant as 35 psu.

We conducted three concurrent simulations using two different adaptive momentum closures; i) *Exp*3 with Laplacian Smagorinsky viscosity (Smagorinsky, 1993), ii) *Exp*4 with Laplacian Leith viscosity (Leith, 1996), iii) *Exp*5 modified Leith which is described below. In the *Exp*3 case, the eddy viscosity is parameterized as

$$\nu_{\text{SM}} = (C_{sm}\,\Delta)^2\,|S|. \tag{17}$$

In this equation, $C_{sm} = \gamma/\pi$ is a non-dimensional Smagorinsky coefficient, $S$ is the deformation rate, and $\Delta$ is the grid spacing. For our simulation, $\Delta$ is the horizontal grid spacing, $\nu_{\text{SM}}$ sets the lateral viscosity, and $\gamma$ is the non-dimensional number which is set to 2.2. In the *Exp*4 and *Exp*5 cases, the eddy viscosity is computed as

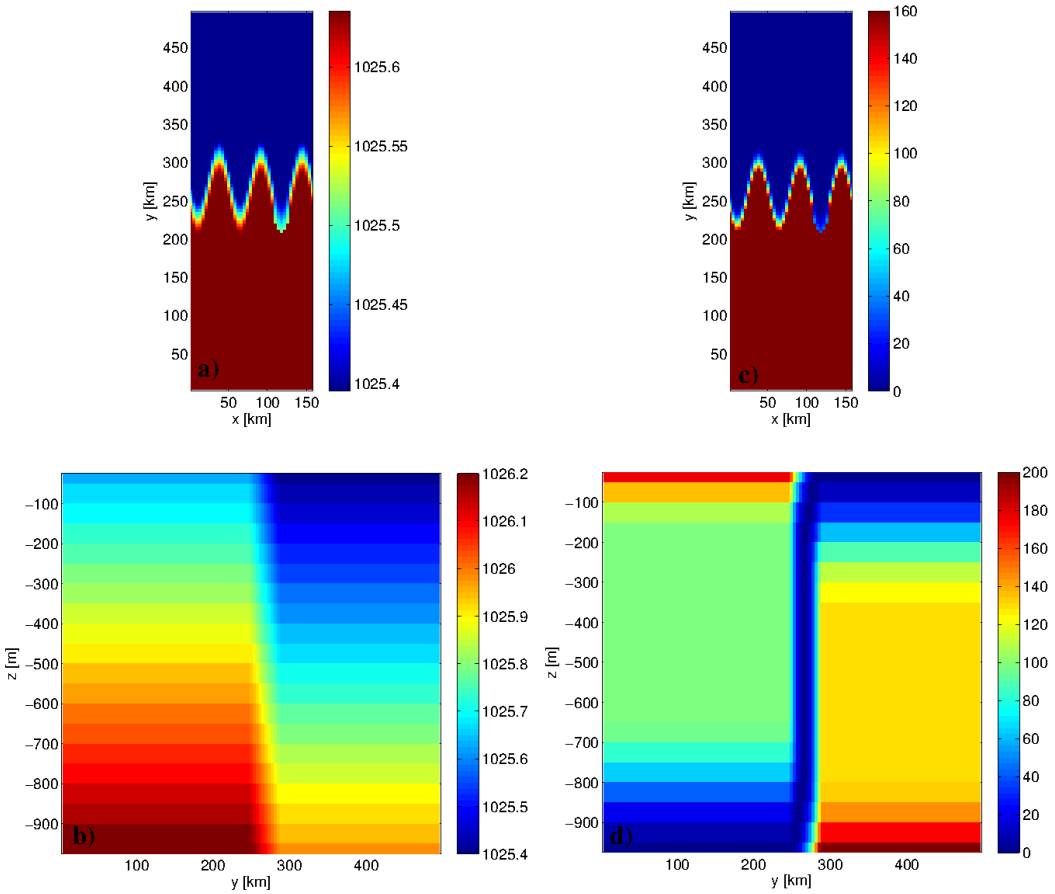


Fig. 6. MITgcm simulation for the BC eddies test case with Smagorinsky viscosity and zero diffusion: (a) horizontal section of density field at time=0 at the surface. (b) vertical section of density field at time=0 at x=80 km. (c) horizontal section of APE field at time=0 at the surface. (d) vertical section of APE field at time=0 at the surface. (d) vertical section of APE field at time=0 at x=80 km.

$$\nu_{\mathrm{LT}} = (C_{lt}\,\Delta)^3\ \sqrt{|\nabla\zeta|^2}, \tag{18}$$

$$\nu_{\mathrm{LTmod}} = (C_{lt}\,\Delta)^3\ \sqrt{|\nabla\zeta|^2 + |\nabla(\nabla\cdot u_h)|}, \tag{19}$$

respectively, where $\zeta$ is the vorticity in the z-direction and $C_{lt} = \gamma/\pi$ is a non-dimensional Leith coefficient. We used the same $\gamma$ parameter for both simulations. The Leith closure can also be expressed as,

$$D_h = \nabla\cdot(\nu_{LT}\nabla\mathbf{u}) = \nabla\cdot(C_{lt}^3\Delta^3|\nabla\zeta|\nabla\,\mathbf{u}\,), \tag{20}$$

where $D_h$ is the horizontal diffusion operator. The right hand side can be written as,

$$D_h = \nu_*\nabla^2\mathbf{u} \tag{21}$$

Using dimensional analysis we get

$$\nu_* = \frac{\nabla \cdot (C_{lt}^3 \Delta^3 |\nabla\zeta| \nabla \mathbf{u})}{\nabla^2 \mathbf{u}} \sim C_{lt}^3 U \frac{\Delta^3}{L^2} \tag{22}$$

Here $L$ is the characteristic length scale. The corresponding grid Reynolds number can be expressed as,

$$Re_\Delta = \frac{U\Delta}{\nu_*} \sim \frac{L^2}{C_{lt}^3 \Delta^2} \tag{23}$$

In the Leith scheme $L$ is proportional to the grid scale, thus the grid Reynolds number can be written as $Re_\Delta = 1/C_{lt}^3$. Note that for the same $\gamma = 2.2$ parameter, grid Reynolds number is approximately 2 and 3 for Smagorinsky and Leith closures, respectively.

In addition to three different momentum closures, we also performed two additional simulations with constant "optimum" laplacian and biharmonic viscosity schemes (*Exp*6 and *Exp*7). We chose 20 $m^2/s$ for the laplacian viscosity which corresponds to approximate grid Reynolds number of 20 (Ilıcak et al., 2012). We also employed the biharmonic viscosity of $4.5 \times 10^8$ $m^2/s$ for the same grid Reynolds number.

Our aim is to test our new method and investigate performance of different momentum closures on spurious mixing. We try to understand in which regions these momentum closures have numerical mixing. Explicit horizontal and vertical diffusions are set to zero in all experiments.

Figures 6 (c) and (d) show horizontal and vertical distribution of the initial available potential energy at the surface and x=80 km, respectively. There is a large APE at the surface and the bottom of the channel due to the large density gradients. The zero APE regions show the neutral density surface at different depths in Fig. 6 (d). After time=0, the flow will adjust to mesoscale eddies due to this available energy and also rotation. We integrated the simulations for 140 days.

Figure 7 (a) shows the density field at depth=625 meter at time=100 days for the *Exp*3 simulation. Mesoscale eddy field with some submesoscale filaments started to develop. The vertical sections of density field at y=250 km and x=80 km are also shown in Figs. 7 (b) and (c), respectively. Dome shaped tilted isopycnals are evidence of baroclinic instabilities and eddies. APE field at depth=625 meter and time=100 days is shown in Fig. 7 (d). There is a high APE anomaly inside the eddy at the center of the domain. The vertical sections of APE at y=250 km and x=80 km are also shown in Figs. 7 (e) and (f), respectively. When we compare Fig. 6 (d) and Fig. 7 (f), we can see that APE between y=150 km and y=350 km is consumed and converted to the kinetic

energy and background potential energy.

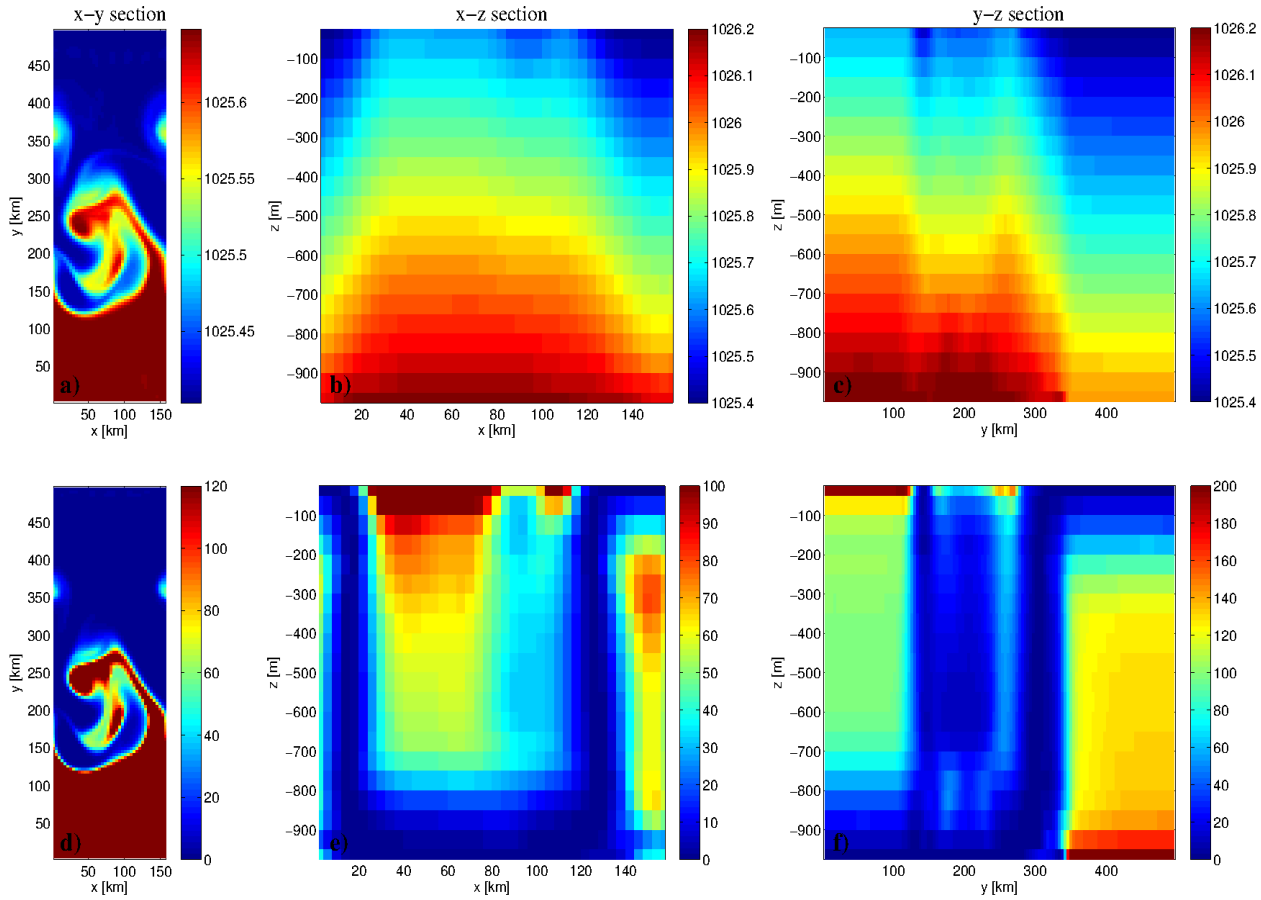


Fig. 7. MITgcm simulation for the BC eddies test case with Smagorinsky viscosity and zero diffusion: (a) horizontal section of density field at time=100 days at depth=625 meter. (b) vertical section of density field at time=100 days at y=250 km. (c) vertical section of density field at time=100 days at x=80 km. (d) horizontal section of APE field at time=100 days at depth=625 meter. (e) vertical section of APE field at time=100 days at y=250 km. (f) vertical section of APE field at time=100 days at x=80 km.

Figures 8 (a) and (c) show the spurious diapycnic mixing between time=100 and 102 days at depth=625 meter for Smagorinsky and Leith viscosity simulations, respectively. The numerical diffusion coincides with border of the mesoscale eddies in both cases. These are the high shear and strain regions. Filaments and stripes of spurious mixing are evident as well. In the Leith case, there is a high spurious mixing region between y=300 km and y=350 km which is absent in the Smagorinsky experiment. The vertical (x-z) section of the total change of $\mathcal{E}_{RPE}$ field is shown in Fig. 8 (b) for *Exp*3 and Fig. 8 (d) for *Exp*4 and at y=150 km. Both experiments exhibit that most of the mixing occurs close to the bottom. We speculate that this might be related to high drag coefficients where the flow creates baroclinic instabilities. Note that we chose the location of this section is different then the section

295 in Figure 7 to display the high numerical mixing regions.

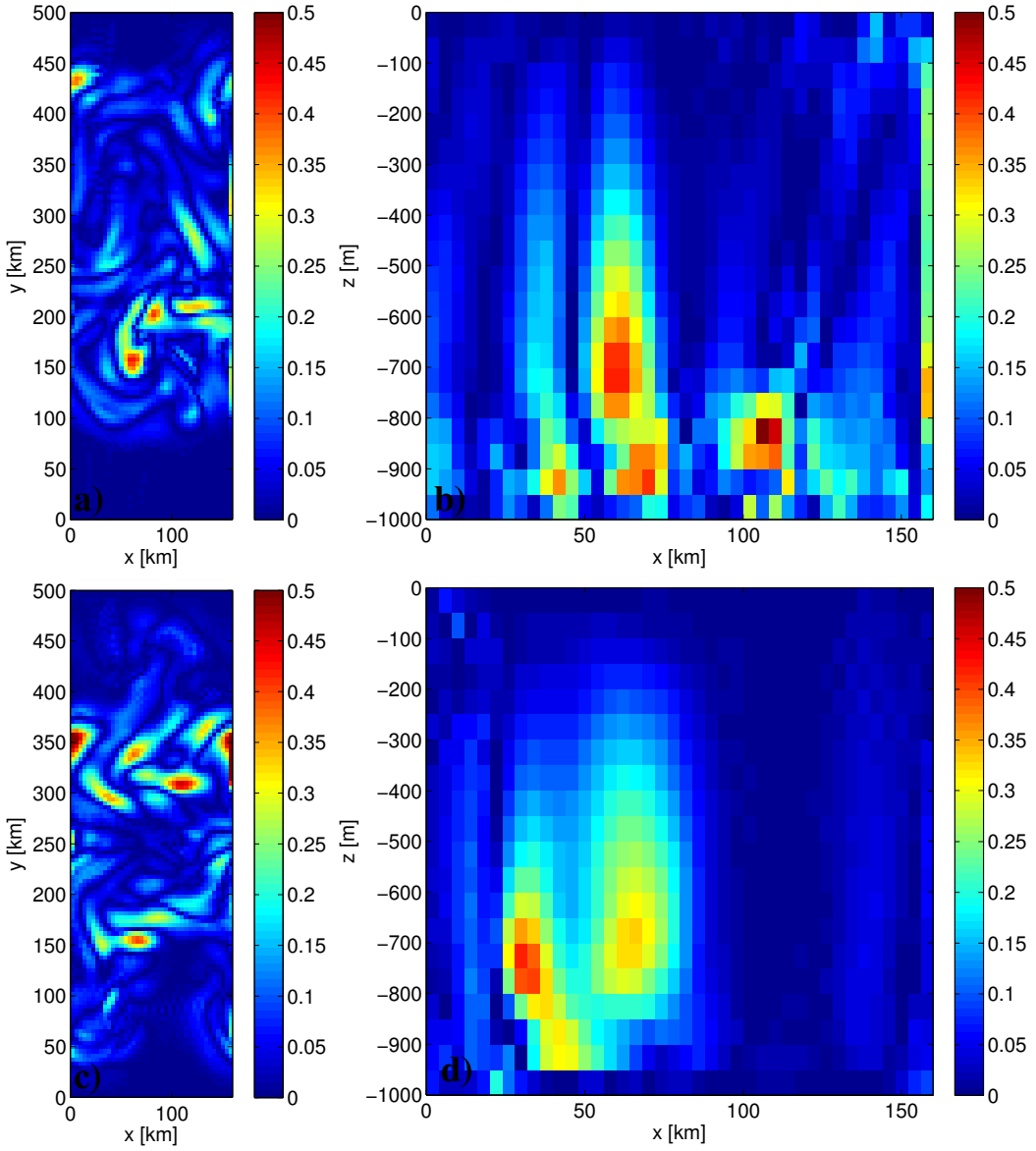


Fig. 8. MITgcm simulation for the BC eddies test case with zero diffusion and Smagorinsky viscosity: (a) horizontal section of spurious mixing field between time=100 and 102 days at depth=625 meter. (b) vertical (x-z) section of spurious mixing field at time=100 days at y=150 km. All units are in kg $m^{-1}s^{-2}$.

296 Last, we show the evolution of reference potential energy for all five sim-
297 ulations in Fig. 9. The *Exp*3 case using the Smagorinsky viscosity has the
298 lowest spurious mixing (red line). The original Leith viscosity case (*Exp*4)
299 has the highest spurious mixing (blue line) between three adaptive momen-
300 tum closures, and spurious mixing in the modified Leith (black line, *Exp*5) is
301 in between *Exp*3 and *Exp*4 cases. Additional term in the Eq. 19 for the Leith
302 viscosity removes the grid noise better than the original version. The orig-
303 inal Leith viscosity only removes vorticity buildup at the grid scale. Thus,

a divergent flow with little or no vertical vorticity can be undamped. The modified Leith version fixes this problem adding a damping of the divergent velocity. It is crucial to show that different momentum closures have different levels of spurious mixing for ocean modelling. In our experiments, original and modified Leith schemes have more numerical mixing than the Smagorinsky closure. The constant Laplacian and biharmonic viscosity schemes (*Exp*6 and *Exp*7) have more spurious mixing than the adaptive closures probably due to slightly higher grid Reynolds numbers. We could have increased the viscosity values in *Exp*6 and *Exp*7 to reduce the numerical mixing, but that would significantly dissipate the mesoscale eddy field and flow becomes more laminar.

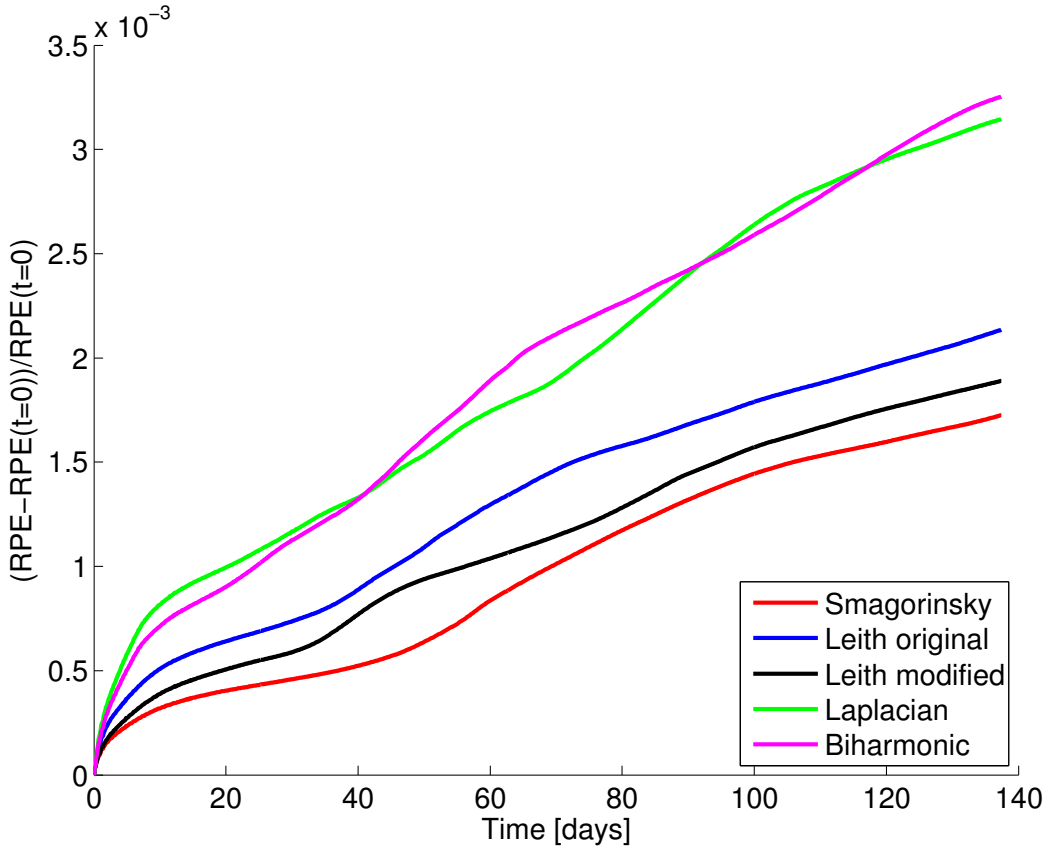


Fig. 9. Evolution of normalized reference potential energy for five different momentum schemes.

## 4 Discussion and conclusions

We propose a new diagnostic method that quantifies the amount and spatial distribution of diapycnic mixing. We call this new method the resting potential energy density method. The method is an extension of the APE density method previously described by Winters and Barkan (2013). The reference

potential energy density is a four dimensional field and the change of $\mathcal{E}_{RPE}$ between two times $(t, t + \Delta t)$ shows regions where absolute reference potential energy increased in the system due to diapycnic mixing. One advantage of this new method is that we can compute changes in energy rather than effective diffusivity. Following reference potential energy gain and loss is useful for diagnosing ocean energy budgets.

We test the new method in a 2D lock-exchange and 3D baroclinic eddy periodic channel test cases. Results are following. In the lock-exchange test case, the new method successfully diagnoses the symmetric spurious mixing regions at the front of the both gravity currents. One of the caveats of the new method is the advection part of the $\mathcal{E}_{RPE}$ which is computed off-line. We also employ the new method using an explicit diffusion and we find that $\mathcal{E}_{RPE}$ can be computed as a combination of explicit and implicit parts. One of the most important results is that the additional explicit diffusivity does not suppress the numerical mixing part.

The impact of three different momentum schemes are also diagnosed using the new scheme for the 3D baroclinic eddies channel case. We use classical Smagorinsky, original Leith and modified Leith viscosity methods. We chose the same non-dimensional coefficient ($C_{sm} = C_{lt} = 2.2$) for all these schemes. $\mathcal{E}_{RPE}$ method shows that most of the spurious mixing in this case is over topography. This might be due to high drag coefficient in the model setup. Further investigation is required, however it is beyond the scope of this paper. In three different momentum schemes, original Leith viscosity has the highest numerical mixing whereas the classical Smagorinsky has the lowest one using the same coefficient. The Leith scheme has slightly larger grid Reynolds number than the Smagorinsky one. However, the main reason behind the high spurious mixing might be that Smagorinsky is based on energy dissipation which removes the grid noise more efficiently, while Leith is based on enstrophy dissipation.

Mesoscale and submesoscale eddies, fronts and filaments are ubiquitous features in the ocean near Western boundary currents, Eastern boundary current upwelling regions and Antarctic Circumpolar Current (ACC). These regions also coincide with large heat exchanges between ocean and atmosphere (i.e. new water formations). Historically, non-eddy resolving (1° degree and higher) and eddy-permitted ($\approx 1/4°$ degree) ocean climate models suffer to preserve water masses in the Arctic Ocean, ACC and mode water formation sites (Ilıcak et al., 2016). This study shows that high shear-strain regions are prone to numerical mixing. This means that not only relatively coarse resolution ocean models, but also regional submesoscale resolved ocean simulations might lead to diapycnic mixing especially lateral/vertical shear and over rough topography areas.

In the future, we would like to test the new method in realistic global ocean models and try to compute regions of spurious mixing. However, effect of topography and connection of different basins raise a challenging question. For instance the Mediterranean Sea is connected to the Atlantic Ocean through only Strait of Gibraltar. Current sorting method does not take into account this water mass separation. We believe combining our method and the method proposed by Stewart et al. (2014) where impact of basin separation in APE field is studied, would be the next step.

## Acknowledgements

M. Ilicak is supported by the SKD BASIC project and Ice2Ice project that has received funding from the European Research Council under the European Community's Seventh Framework Programme (FP7/2007-2013) / ERC grant agreement no 610055.

## Appendix

Advection of reference potential energy density, $\mathcal{E}_{RPE}$, in time has to be removed from the total change of $\mathcal{E}_{RPE}$ to locate the spurious mixing regions. The material derivative of $\mathcal{E}_{RPE}$, can be expressed as

$$\frac{d\mathcal{E}_{RPE}}{dt} = \frac{\partial z^*}{\partial t}\rho - u \cdot \nabla \rho z^* + \frac{\partial \int \rho(z^{*'})dz^{*'}}{\partial t},$$

where $z^*$ is the sorted state and $\rho$ is the density.

## References

Burchard, H., Rennau, H., 2008. Comparative quantification of physically and numerically induced mixing in the ocean models. Ocean Modell. 20, 293–311.

Griffies, S. M., Pacanowski, R. C., Hallberg, R. W., 2000. Spurious Diapycnal Mixing Associated with Advection in a z-Coordinate Ocean Model. Mon. Wea. Rev. 128, 538–564.

Haidvogel, D. B., Beckmann, A., 1999. Numerical ocean circulation modeling. Imperial College Press.

Hughes, G. O., Hogg, A. M., Griffiths, R. W., 2009. Available Potential Energy and Irreversible Mixing in the Meridional Overturning Circulation. Journal of Physical Oceanography 39, 3130.

Ilıcak, M., Adcroft, A. J., Griffies, S. M., Hallberg, R. W., 2012. Spurious dianeutral mixing and the role of momentum closure. Ocean Modelling 45, 37–58.

Ilıcak, M., Drange, H., Wang, Q., Gerdes, R., Aksenov, Y., Bailey, D. A., Bentsen, M., Biastoch, A., Bozec, A., Böning, C., Cassou, C., Chassignet, E., Coward, A. C., Curry, B., Danabasoglu, G., Danilov, S., Fernandez, E., Fogli, P. G., Fujii, Y., Griffies, S. M., Iovino, D., Jahn, A., Jung, T., Large, W. G., Lee, C., Lique, C., Lu, J., Masina, S., Nurser, A. J. G., Rabe, B., Roth, C., Salas y Mélia, D., Samuels, B. L., Spence, P., Tsujino, H., Valcke, S., Voldoire, A., Wang, X., Yeager, S. G., Mar. 2016. An assessment of the Arctic Ocean in a suite of interannual CORE-II simulations. Part III: Hydrohraphy and fluxes. Ocean Modelling 100, 141–161.

Ilıcak, M., Özgökmen, T. M., Özsoy, E., Fischer, P. F., 2009. Non-hydrostatic modeling of exchange flows across complex geometries. Ocean Model. 29, 159–175.

IOC, SCOR, IAPSO, 2010. The international thermodynamic equation of seawater-2010: calculation and use of thermodynamic properties. Intergovernmental Oceanographic Commission, Manuals and Guides No. 56, UNESCO, available from http://www.TEOS-10.org, 196pp.

Leith, C. E., 1996. Stochastic models of chaotic systems. Physica D. 98, 481–491.

Marshall, J., Adcroft, A., Hill, C., Perelman, L., Heisey, C., 1997. A finite-volume, incompressible Navier Stokes model for studies of the ocean on parallel computers. Journal of Geophysical Research 102, 5753–5766.

McDougall, T. J., 1987. Thermobaricity, cabbeling, and water-mass conversion. Journal of Geophysical Research 92, 5448–5464.

Petersen, M. R., Jacobsen, D. W., Ringler, T. D., Hecht, M. W., Maltrud, M. E., Feb. 2015. Evaluation of the arbitrary Lagrangian-Eulerian vertical coordinate method in the MPAS-Ocean model. Ocean Modelling 86, 93–113.

Smagorinsky, J., 1993. Some historical remarks on the use of nonlinear viscosities. In: Galperin, B., Orszag, S. A. (Eds.), Large Eddy Simulation of Complex Engineering and Geophysical Flows. Cambridge University Press, pp. 3–36.

Stewart, K. D., Saenz, J. A., Hogg, A. M., Hughes, G. O., Griffiths, R. W., Apr. 2014. Effect of topographic barriers on the rates of available potential energy conversion of the oceans. Ocean Modelling 76, 31–42.

Urakawa, L. S., Hasumi, H., Feb. 2014. Effect of numerical diffusion on the water mass transformation in eddy-resolving models. Ocean Modelling 74, 22–35.

Winters, K. B., Barkan, R., Jan. 2013. Available potential energy density for Boussinesq fluid flow. Journal of Fluid Mechanics 714, 476–488.

Winters, K. B., Lombard, P. N., Riley, J. J., D'Asaro, E. A., Apr. 1995. Available potential energy and mixing in density-stratified fluids. Journal of Fluid Mechanics 289, 115–128.